

**Relativistic First-Principles Full Potential Calculations of  
Electronic and Structural Properties of group IIIA-VA  
semiconductors based on Zeroth Order Regular Approximation  
(ZORA) Hamiltonian.**

Eugene S. Kadantsev

*Quantum Theory Group, Institute for Microstructural Sciences,  
National Research Council, Ottawa, Canada K1A 0R6\**

(Dated: December 9, 2021)

Abstract

First-principles full potential calculations based on Zeroth Order Regular Approximation (ZORA) relativistic Hamiltonian and Kohn-Sham form of Density Functional Theory (KS DFT) in local spin density approximation (LSDA) are reported for group IIIA-VA (InAs, GaAs, InP) semiconductors. The effects of relativity are elucidated by performing fully relativistic, scalar relativistic, and nonrelativistic calculations. Structural and electronic band structure parameters are determined including split-off energies, band gaps, and deformation potentials. The nature of chemical bonding at the equilibrium and under hydrostatic strain is investigated using projected (PDOS) and overlap population weighted density of states (OPWDOS). ZORA results are compared with Augmented Plane Wave plus Local Orbitals method (APW+lo), and experiment. Viability and robustness of the ZORA relativistic Hamiltonian for investigation of electronic and structural properties of semiconductors is established.

PACS numbers:

---

\*Electronic address: ekadants@babylon.phy.nrc.ca

## I. INTRODUCTION

There is a great interest in electronic and structural properties of group IIIA-VA materials due to their wide spread applications in semiconductor devices. In particular, InAs/GaAs and InAs/InP semiconductor quantum dots (QDs) [1] have shown great promise [2] in quantum information applications such as is the generation of entangled photon pairs (EPPs) on demand [3–6].

Atomistic modeling of semiconductor nanostructures may require input from accurate Density Functional [7–9] calculations in cases when experimental data is not available. Therefore, it is important to understand which material parameters are well reproduced with “standard DFT” and this work is a contribution in this area. Three factors determine accuracy of Density Functional calculations 1) Model exchange-correlation functional; 2) Representation of single-particle orbitals (atomic orbitals, plane-waves, real space grids) and representation of ion-electron interaction (*ab initio* pseudopotentials, full potential schemes); 3) Treatment of relativity. The assessment of the accuracy of exchange-correlation functionals is beyond the scope of this contribution. The main objective of this work is to perform a detailed study of structural and electronic structure properties of InAs, InP, and GaAs semiconductors using highly accurate representation of single-particle orbitals and ion-electron interaction and to assess the role of relativity in these calculations.

First-principles calculations on group IIIA-VA semiconductors based on Kohn-Sham form of Density Functional Theory [7–9] have already been performed in the past [10–15]. The computational approach used in these calculations generally evolved from *ab initio* pseudopotential calculations to more elaborate full potential (FP) augmentation schemes [16–19] such as Linearized Augmented Plane Wave (LAPW) and Augmented Plane Wave plus local orbitals (APW+lo) methods. LAPW and APW+lo have now become the methods of choice when accuracy considerations have the highest priority.

There is also a less known full potential method due to te Velde and Baerends [20, 21] which makes use of Bloch basis set made up of numerical and Slater type atomic orbitals (NAO/STO basis), a basis which is excellent for the accurate representation of the electron density. The approach due to te Velde and Baerends is implemented in BAND program [22] and is capable of treating chemical elements throughout periodic table using Zeroth Order Regular Approximation (ZORA) relativistic Hamiltonian [23–27]. ZORA approach is

designed to capture scalar relativistic effects such as  $s$  and  $p$  “orbital contraction” (stabilization) and  $d$  “orbital expansion” (destabilization) as well as spin-orbital splitting for electrons with angular momentum  $l > 0$ . While ZORA Hamiltonian is very well established among quantum chemists, relativistic ZORA calculations on solids are much less common [28–33], especially, in comparison with a large volume of calculations employing LAPW and APW+lo methods. Therefore, further assessment of ZORA performance in solids is important.

In this work, I will employ ZORA Hamiltonian to perform a detailed study of structural and electronic band structure properties of InAs, InP, and GaAs semiconductors in zinc-blende phase. The effects of relativity are elucidated by performing three sets of calculations 1) nonrelativistic 2) scalar relativistic and 3) relativistic with variational treatment of spin-orbital coupling (or fully relativistic). ZORA Hamiltonian is applied to calculate electronic band structures, band gaps, and deformation potentials. The results obtained with ZORA Hamiltonian are compared to those obtained with APW+lo method, and with experiment.

I perform a detailed analysis of electronic structure of InAs, InP and GaAs in terms of Projected and Overlap Population Weighted Density of States (PDOS/OPWDOS analysis). Whereas it is a relatively general practice to report and discuss PDOS, the usage OPWDOS is much less common. The OPWDOS analysis, popularized [34] by the Nobel Prize winner Roald Hoffmann, provides a clear pictorial representation of bonding, non-bonding, and anti-bonding orbital interactions and is deemed useful. I will demonstrate the usage of OPWDOS plots and explain how they add to our understanding of chemical bond in InAs, InP, and GaAs.

Atomic units  $\hbar = e = m_e = 1$  are used throughout unless otherwise specified.

## II. COMPUTATIONAL APPROACH

The first-principles KS DFT calculations with ZORA Hamiltonian are carried out with BAND program [20–22]. BAND makes use of periodic boundary conditions (PBC) and explicit Bloch basis composed of numerical and Slater type atomic orbitals (NAO/STAO basis). I also perform calculations with APW+lo method [16, 17] as implemented in EXCITING program [35]. Both methods are capable of including spin-orbital coupling variationally and I choose to do so. To clarify effects of relativity, I also present results of scalar relativistic and nonrelativistic calculations.

The relativistic effects in BAND are treated in the Zeroth Order Regular Approximation (ZORA) approach of van Lenthe and co-workers [23–27]. The details of ZORA implementation in BAND are given in Ref. [29]. In ZORA approach, the kinetic energy operator is replaced by the ZORA expression  $\hat{T}^{ZORA}$

$$-\frac{1}{2}\mathbf{p}^2 \Rightarrow \hat{T}^{ZORA} = \vec{\sigma} \cdot \mathbf{p} \frac{c^2}{2c^2 - V_{SAPA}(\mathbf{r})} \vec{\sigma} \cdot \mathbf{p}, \quad (1)$$

where  $\mathbf{p}$  is the “momentum operator” ( $\mathbf{p} = -i\nabla$  in the absence of a magnetic field);  $V_{SAPA}(\mathbf{r})$  – is a sum of atomic potentials (SAPA), an approximation to the total effective potential in the ZORA kinetic energy operator; and  $\vec{\sigma} = \{\sigma_x, \sigma_y, \sigma_z\}$  – is a vector made up of the Pauli matrices. Introducing the notation

$$K = \frac{1}{1 - V_{SAPA}(\mathbf{r})/2c^2}, \quad (2)$$

the ZORA kinetic energy becomes

$$\hat{T}^{ZORA} = \vec{\sigma} \cdot \mathbf{p} \frac{K}{2} \vec{\sigma} \cdot \mathbf{p} = \mathbf{p} \frac{K}{2} \mathbf{p} + \frac{1}{2} \vec{\sigma} \cdot (\nabla K \times \mathbf{p}). \quad (3)$$

In the last equation,  $\hat{T}^{ZORA}$  was split into the so-called scalar relativistic  $\hat{T}_{SR}^{ZORA}$  and spin-orbital  $\hat{T}_{SO}^{ZORA}$  terms, where  $\hat{T}_{SO}^{ZORA} = 1/2 \vec{\sigma} \cdot (\nabla K \times \mathbf{p})$ . The nonrelativistic limit can be obtained by setting  $K \rightarrow 1$ . I will refer to calculations with  $\hat{T}^{ZORA}$ ,  $\hat{T}_{SR}^{ZORA}$ , and  $K = 1$  as (fully) relativistic (ZORA FREL), scalar relativistic (ZORA SREL), and nonrelativistic (NREL), respectively.

In my BAND calculations, I use basis set of triple zeta quality (TZ2P in BAND’s notation) taken from the program’s database. The core states are obtained from the full potential atomistic calculations and are kept frozen during the self consistent field (SCF) procedure. The valence states are expanded in terms of the NAO/STAO Bloch basis set functions orthogonalized on the core states (VOC basis). The Hamiltonian matrix elements are evaluated using highly accurate numerical integration scheme [36]. The Brillouin zone integration is carried out using accurate quadratic tetrahedron method [37, 38] with 65 symmetry unique  $\mathbf{k}$ -points spanning the irreducible Brillouin zone (IBZ). The “default” convergence criteria are used to terminate the SCF procedure.

APW+lo calculations are carried out with EXCITING program [35]. The local orbitals and linearization energies are taken from the program’s database. The “core” states are treated fully relativistically and self-consistently in the spherical approximation, whereas the

“valence” states are treated using the second-variational Hamiltonian. The IBZ is sampled using  $\{8 \times 8 \times 8\}$  uniform mesh of  $\mathbf{k}$ -points.

The exchange-correlation is treated within the local spin density approximation (LSDA) [8, 9]. BAND and APW+lo LSDA calculations are carried out using Vosko-Wilk-Nusair [39] and Perdew-Wang [40] parameterization of the correlation energy, respectively. The calculations are performed using “primitive” face-centered cubic cell with two atoms per cell. The zinc-blende crystal structure was assumed.

The structural parameters are obtained by varying the lattice constant (from -20 to 20% of the equilibrium volume) and fitting the total energies to the Murnaghan equation of state [41].

The electronic structure is analyzed using projected density of states (PDOS) and overlap population weighted density of states (OPWDOS). PDOS is defined for a function  $\chi_\mu$  or a set of functions  $\{\chi_\mu\}$  and has large values at energies where  $\chi_\mu$  (or  $\{\chi_\mu\}$ ) has large contributions in eigenstates (bands, molecular orbitals). PDOS can also be large in energy intervals with a large number of states. The weights in my PDOS are derived from Mulliken population analysis [42, 43]. The  $i$ th eigenstate of the Kohn-Sham Hamiltonian  $\psi_{i\mathbf{k}}$  is expanded in a finite basis

$$\psi_{i\mathbf{k}}(\mathbf{r}) = \sum_{\mu} c_{\mu i}(\mathbf{k}) \chi_{\mu\mathbf{k}}(\mathbf{r}), \quad (4)$$

where  $c_{\mu i}(\mathbf{k})$  are expansion coefficients and  $\chi_{\mu\mathbf{k}}$  are basis set functions – Bloch sums of equivalent atomic orbitals. The gross population of  $\chi_{\mu\mathbf{k}}$  for the eigenstate  $\psi_{i\mathbf{k}}$  is

$$GP_{i\mathbf{k}}(\chi_{\mu\mathbf{k}}) = \frac{1}{2} \sum_{\nu} \left( c_{\mu i}(\mathbf{k}) c_{\nu i}^{\dagger}(\mathbf{k}) S_{\mu\nu}(\mathbf{k}) + c_{\mu i}^{\dagger}(\mathbf{k}) c_{\nu i}(\mathbf{k}) S_{\nu\mu}(\mathbf{k}) \right) \quad (5)$$

and PDOS for function  $\chi_\mu$  is

$$PDOS_{\chi_\mu}(E) = \sum_i \sum_{\mathbf{k}} GP_{i\mathbf{k}}(\chi_{\mu\mathbf{k}}) L(E - E_{i\mathbf{k}}), \quad (6)$$

where  $E_{i\mathbf{k}}$  is Kohn-Sham eigenvalue corresponding to eigenstate  $\psi_{i\mathbf{k}}$  and  $L$  is a Lorentzian broadening function.

OPWDOS is defined for two functions  $\chi_\mu$  and  $\chi_\nu$  or between two sets of functions ( $\{\chi_\mu\}$  and  $\{\chi_\nu\}$ ) and has large positive or negative values depending on whether the interaction between  $\chi_\mu$  and  $\chi_\nu$  ( $\{\chi_\mu\}$  and  $\{\chi_\nu\}$ ) is bonding or anti-bonding, respectively. The use of these plots is demonstrated in Ref. [44]. The overlap population of two orbitals and

OPWDOS are defined as

$$\begin{aligned}
 OP_{i\mathbf{k}}(\chi_{\mu\mathbf{k}}, \chi_{\nu\mathbf{k}}) &= c_{\mu i}(\mathbf{k})c_{\nu i}^\dagger(\mathbf{k})S_{\mu\nu}(\mathbf{k}) + c_{\mu i}^\dagger(\mathbf{k})c_{\nu i}(\mathbf{k})S_{\nu\mu}(\mathbf{k}), \\
 OPWDOS_{\chi_{\mu}, \chi_{\nu}}(E) &= \sum_i \sum_{\mathbf{k}} OP_{i\mathbf{k}}(\chi_{\mu\mathbf{k}}, \chi_{\nu\mathbf{k}})L(E - E_{i\mathbf{k}}).
 \end{aligned}
 \tag{7}$$

### III. RESULTS

#### A. InP, GaAs, and InAs: Structural Parameters

Fig. 1 shows energy level diagram for “spherically symmetric” In, As, Ga, and P atoms. Fig. 1 shows that group IIIA atomic species In and Ga have smaller  $ns - np$  and  $ns - (n - 1)d$  energy spacings as compared to group VA species (As and P). The  $s - p$  energy spacings are 5.7–6.4 eV for In and Ga and 9.3–8.4 eV for As and P, respectively.

InP, GaAs, and InAs are known to exist in several phases (See Refs. [10, 45] and the references therein). The low pressure phase of all three (GaAs, InP, InAs) semiconductors is zinc-blende. While there had been some discussions on the nature of the first high pressure phase of GaAs, it is now generally agreed that the first transition takes place at approximately 17 GPa and involves transition from zinc-blende (GaAs-I) to orthorhombic  $Cmcm$  phase (GaAs-II) [46]. The pressure release results in a transition to a cinnabar phase followed by a transition to the original zinc-blende phase [47]. No direct zinc-blende to cinnabar transition was observed. The first high-pressure phase in common “cation” InP and InAs was experimentally found to be NaCl phase [48–50]. The latter finding is supported by Density Functional calculations [51, 52].

In connection with InAs quantum dots in GaAs or InP matrix, the low pressure zinc-blende phase (Strukturbericht designation  $B3$ ) is of primary interest. The structural parameters of InP, GaAs, and InAs obtained from my Density Functional calculations with ZORA Relativistic Hamiltonian and APW+lo method are summarized in Table I. Table I also shows experimental values [45] which were measured at room temperature and the results of APW+lo calculations. Figure 2 shows the deviations between LSDA lattice constants and the experimental lattice constants.

The finite temperature effects will increase the lattice constant. Once these temperature effects are taken into account, the “experimental” lattice constant is effectively reduced which will influence the conclusions about the accuracy of a given exchange-correlation functional.

For example, in the case of GaAs, the temperature effects lead to the increase in the lattice constant by 0.3% from 5.638 Å to 5.653 Å [53]. Since LSDA underestimates [53, 54] the bond lengths, the inclusion of finite temperature effects into consideration will improve the agreement between the theory and experiment.

Table I and Figure 2 show that LSDA ZORA relativistic and scalar relativistic results underestimate the lattice constants by, approximately, 0.6% (InP), 0.8 % (GaAs), and 0.5 % (InAs). The consideration of finite temperature effects will further improve agreement between the theory and experiment and it is likely that the error of LSDA relativistic ZORA calculation for lattice constants is within 0.5%.

In agreement with the established trend [55], the relativity contracts the bond length. The DFT lattice constant decreases as the treatment of relativity changes from “nonrelativistic” (NREL) to fully relativistic (FREL). Variational treatment of spin-orbital coupling does not seem to affect the structural properties by much, the reduction in the equilibrium lattice constant upon going from SREL to FREL is very small (within 0.05%). It is important to include some kind of description of relativity for In – NREL lattice constants for InP and InAs are larger than experimental ones which contradicts to the established LSDA trend [53, 54].

Figure 3 shows LSDA bulk modulus calculated at different “levels of relativity” (FREL - fully relativistic with variational treatment of spin orbital coupling, SREL - scalar relativistic, and NREL - nonrelativistic). My LSDA calculations reproduce the “stiffness” trend  $B_{InAs} < B_{InP} < B_{GaAs}$ . The bulk modulus decreases upon going from NREL to SREL description and, then, slightly increases by going from SREL to FREL. In the case of InP and GaAs, the LSDA bulk modulus  $B_{LSDA}$  is smaller (less stiffer) than the experimental bulk modulus. This seems to contradict to the “established” LSDA trend of  $B_{LSDA}$  being too stiff, note, however, that by examining Table V of Ref. [53] one can not conclude this with respect to group IVA and group IIIA-VA semiconductors. In the case of InAs, ZORA FREL and SREL bulk modulus is by 2% more stiffer than the experimental bulk modulus.

I find that my APW+lo calculations are in good agreement with the ZORA calculations. The APW+lo lattice constants are within 0.2% of the ZORA lattice constants. The bulk moduli obtained from the APW+lo calculations are smaller than those obtained with BAND program (FREL) by 2 %, 6%, and 15% for InP, GaAs, and InAs, respectively, but the “stiffness” trend  $B_{InAs} < B_{InP} < B_{GaAs}$  is reproduced.

## B. InP, GaAs, and InAs: PDOS and OPWDOS Analysis

Figs. 4, 6, and 8 show relativistic PDOS for InP, GaAs, and InAs, respectively. The PDOS is calculated at three values of the lattice constant corresponding to the tensile hydrostatic strain (Figs. (a) and (b)), equilibrium (Figs. (c) and (d)), and compressive hydrostatic strain (Figs. (e) and (f)).

Let us consider PDOS at the equilibrium (experimental) lattice constants in InP, GaAs, and InAs (middle rows of Figs. 4, 6, and 8). The left (c) and right (d) columns show PDOS on the cation (In, Ga) and anion (As, P) atomic orbitals (AOs), respectively. The names “cation” and “anion” reflect the move away from covalent bonding and towards ionicity in InP, GaAs, and InAs semiconductors. The Hirshfeld charge analysis [56] performed in this work reveals that electron density transfers from regions near In and Ga ions into regions near As and P ions making In and Ga “positively” and As and P “negatively” charged, respectively.

We find that PDOS of InP, GaAs, and InAs in the valence band energy region (up to 16 eV below the Fermi energy, the Fermi energy is at zero) consists of four main “spectral features”.

The first “spectral feature” in the PDOS is a peak of broad character just below the Fermi energy. The width of this peak is, approximately, 3.2 eV for InAs and InP and 4.4 eV for GaAs. The main contribution to this “spectral feature” stems from anion and, to a lesser extent, from cation atomic orbitals (AOs) of  $p$  type. There is a small contribution from  $s$  and  $d$  cation orbitals and, in the case of GaAs and InAs,  $s$  and  $d$  anion orbitals.

The second feature is a very sharp peak centered around 5.4 eV (InAs, InP) and 6.5 eV (GaAs) below the Fermi energy. The main contributions to this peak are cation AOs of  $s$  type. The smaller contributions to this peak are arising from anion and cation AOs of  $p$  type. The second feature has a slowly decaying tail which contributes to the very top of the valence band.

The third peak in the PDOS is located, approximately, at 9.5 eV (InP), 12.2 eV (GaAs), and 10.9 eV (InAs) below the Fermi energy. The main contribution to this peak stem from anion  $s$  type orbitals as well as from cation  $p$ ,  $s$  and  $d$  AOs. The last “spectral feature” is a very sharp peak in the PDOS due to the cation  $d$  orbitals and anion  $s$  type orbitals.

The PDOS in the conduction band energy region is shown up to 9.5 eV above the Fermi

energy and consists of several closely spaced peaks. The main contributions in this energy window are the anion  $p$  and  $d$  and cation  $p$ ,  $s$ , and  $d$  AOs. The PDOS does not show significant anion  $s$ -type contributions in the conduction band region.

Figs. (a),(b) and (c),(d) demonstrate the effect of the hydrostatic tensile and compressive strains on the PDOS. The compressive hydrostatic strain 1) broadens PDOS peaks; 2) decreases magnitude of the PDOS peaks; 3) changes the relative position of the peaks. The “general structure” of the PDOS is preserved.

Figs. 5, 7, and 9 show OPWDOS for InP, GaAs, and InAs, respectively. The OPWDOS is calculated at the experimental equilibrium lattice constants and provides a clear pictorial representation of orbital interactions in IIIA-VA InP, GaAs, and InAs zinc-blende semiconductors.

The OPWDOS in the valence band energy region is of mostly bonding character. The OPWDOS shows that the very top of the valence band is strongly stabilized by cation-anion  $p - p$  orbital interactions. The energy region corresponding to the second PDOS peak is characterized by the cation  $s$  - anion  $p$  and cation  $p$  - anion  $s$  bonding interactions as well as a slightly anti-bonding cation  $s$  - anion  $s$  interactions. The energy region corresponding to the third PDOS peak is characterized by the cation  $p$  - anion  $s$  interaction.

The OPWDOS in the conduction band energy region is mostly of the anti-bonding character and has peaks that are generally higher in magnitude than the OPWDOS peaks in the valence band region. The latter is a demonstration of a well known fact that the “anti-bonding is more anti-bonding than bonding is bonding” (see Ref. [57] and the references therein). The bottom of the conduction band is strongly “destabilized” by cation-anion  $s - p$ ,  $p - s$ , and  $s - s$  interactions. It is interesting to note that the cation-anion  $p - p$  interaction for the very bottom of the conduction band (within 1 eV) is bonding. At the higher energies, the  $p - p$  interaction becomes strongly anti-bonding.

### C. InP, GaAs, and InAs: Electronic Structure Parameters

The PDOS and OPWDOS presented in Section IIIB describe the electronic structure qualitatively. Tables II and IV show results for the parameters of the electronic structure for InP, GaAs, and InAs IIIA-VA zinc-blende semiconductors. These parameters are the band gaps for the transitions between the high-symmetry points of the Brillouin zone  $E_{gap}^{1 \rightarrow 2} =$

$E_2 - E_1$ , split-off energies at the  $\Gamma$  and  $L$  points of the Brillouin zone, position (with respect to the Fermi energy) and width of the cation  $d$ -band at the  $\Gamma$  point, and the width of the upper part of the valence band. Table IV summarizes the relative volume deformation potentials for a specific  $1 \rightarrow 2$  transition defined as

$$a_V^{1 \rightarrow 2} = \frac{dE_{21}}{d \ln V}. \quad (8)$$

The electronic band structure parameters are computed at several levels of relativity (FREL - fully relativistic, SREL - scalar relativistic, and NREL - nonrelativistic) as well as with the APW+lo method (fully relativistic approach). The results of these calculations are compared with available experimental data.

In agreement with previous work, Table II shows that LSDA KS DFT severely underestimates band gaps. The small LSDA band gap becomes even smaller when one introduces explicit description of relativity. For example, in the case of GaAs, the direct gap  $E_{gap}^{\Gamma_V \rightarrow \Gamma_C}$  decreases from 1.0 eV to 0.4 eV as the “level of relativity” changes from nonrelativistic to fully relativistic. The relativity especially strongly affects band gaps at  $\Gamma$  and  $L$  points of the Brillouin zone.

In the Table III, I summarized orbital populations for three top valence bands (split-off  $\Gamma_{7v}$ , light-hole, and heavy hole  $\Gamma_{8v}$ ) and the lowest conduction band ( $\Gamma_{6c}$ ) at the high-symmetry points of the Brillouin zone. From Table III, one can see that the bottom of the conduction band at the  $\Gamma$  and  $L$  points has significant contributions from cation  $s$ -type AOs, whereas at the  $X$  point the bottom of the conduction band is made up of cation  $p$ -type orbitals. The reason for the strong “relativistic” band gap decrease at the  $\Gamma$  and  $L$  points is that the conduction  $s$  states are stabilized by relativity stronger than the valence  $p$  states. The stabilization itself stems from the relativistic “contraction” of the atomic orbitals [58]. Overall, the gaps in the relativistic description decrease substantially which might affect the conclusions with respect to the accuracy of a given exchange-correlational functional for the band gap calculation.

For a fixed lattice constant, LSDA also poorly describes the energy differences within the conduction band. For example,  $E(X_C) - E(L_C)$  energy difference is 508 meV from ZORA FREL calculations, whereas the experimental value is 160 meV. The relative position of the conduction band minima is described only qualitatively  $E_{gap}^{\Gamma_V \rightarrow \Gamma_C} < E_{gap}^{\Gamma_V \rightarrow L_C} < E_{gap}^{\Gamma_V \rightarrow X_C}$ .

The strong underestimation of the band gaps may result in the wrong energetic order of

bands in some specific points of the Brillouin zone. This happens at the  $\Gamma$  point for InAs at the equilibrium lattice constant, where a conduction band  $\Gamma_{6c}$  is strongly stabilized and lies below the split-off band  $\Gamma_{7v}$ . The strain also may affect the energetic order of bands.

Figures 10 and 11 show scalar relativistic and fully relativistic band structure plots for InP, GaAs, and InAs, respectively. The band structure is computed along the edges connecting the high-symmetry points of the Brillouin zone. The Cartesian coordinates of these high-symmetry points are summarized in Table V. From these band structure plots one can see the band crossing at the  $\Gamma$ -point for InAs at the equilibrium lattice constant. This band crossing also occurs in InP and GaAs subjected to the tensile hydrostatic strain.

It is found that the split-off energies at the  $\Gamma$  and  $L$  points are reproduced very accurately within ZORA fully relativistic approach, the agreement with the experiment is a few % or several meVs. The fully relativistic treatment for the calculation of the split-off energies is essential as both scalar relativistic/nonrelativistic calculations lead to the six-fold (including spin) degeneracy of the valence band at the  $\Gamma$ -point (Fig. 10).

The relative volume deformation potential describes how fast a given band gap changes with volume. The negative (positive) relative deformation potential (in our definition) means that the band gap increases (decreases) as volume decreases. Table II shows that for both  $\Gamma_V \rightarrow \Gamma_C$  and  $\Gamma_V \rightarrow L_C$  transitions, both gaps are increasing as volume decreases (negative deformation potential), whereas for the  $\Gamma_V \rightarrow X_C$  transition, the band gap decreases (the deformation potential is positive). The differences in the sign of the deformation potential for  $\Gamma_V \rightarrow \Gamma_C$  and  $\Gamma_V \rightarrow L_C$  transitions on one hand and  $\Gamma_V \rightarrow X_C$  transition on the other hand are attributed to the “different nature” of the conduction band minimum at these points (see Table III).

The calculated absolute magnitude of the “rate of change” in the gap is the largest for GaAs and decreases for semiconductors with a larger lattice constant (InP, InAs). The experimental relative deformation potentials are obtained from the direct band gap pressure dependence coefficients and experimental bulk moduli. The experimental trend in the absolute magnitude of the “rate of change” in the gap is GaAs, InAs, and InP. Note, however, that experimental uncertainties for the relative deformation potential can be as large as 1 eV. The relative deformation potentials are quite close for fully relativistic and scalar relativistic calculations and, therefore, a fully relativistic calculation of this quantity does not seem essential, at least, for the transitions considered in this work.

Finally, there are two other quantities which sensitively depend on fully relativistic calculation – the cation  $d$ -band width and the width of the upper part of the valence band UVBW. Both band widths increase as the treatment of relativity changes from non-relativistic to fully relativistic level. For UVBW, the increase is 6%-8% (0.4-0.5 eV). The  $d$ -band width increases dramatically from 0.10-0.15 eV to 0.9 eV.

The agreement between ZORA fully relativistic and APW+lo calculations is exceptionally good, especially, for the relative deformation potentials,  $E_d^\Gamma$ ,  $\delta E_d^\Gamma$ , and for UVBW. The split-off energies are reproduced within 10 meVs, and the gaps usually agree within 20 meVs.

#### IV. CONCLUSIONS

First-principles full potential calculations based on the Zeroth Order Regular Approximation (ZORA) relativistic Hamiltonian and the Kohn-Sham form of Density Functional Theory (KS DFT) were reported for group IIIA-VA (InAs, GaAs, InP) semiconductors. The effects of relativity were elucidated by performing fully relativistic, scalar relativistic, and nonrelativistic calculations. The inclusion of relativity led to the contraction of the bond length, strong stabilization of the conduction band at  $\Gamma$  and  $L$  points of the Brillouin zone, and broadening of the upper part of the valence band. The inclusion of relativity at least on the scalar relativistic level was found to be essential for the accurate calculation of structural properties. Electronic band structure parameters were determined including split-off energies, band gaps, deformation potentials, and populations at the high-symmetry points of the Brillouin zone. It was found that the split-off energies can be determined with very good accuracy. In agreement with previous work, LSDA KS DFT severely underestimates band gaps which may result in the wrong energetic order of bands at specific points of the reciprocal space. It was found that relativistic LSDA describes the sequence of conduction band minima only qualitatively. The relative band gap deformation potentials were determined and compared with the available experimental data. The relativistic LSDA relative deformation potentials at the  $\Gamma$  point were found to be too small. The nature of the chemical bonding at the equilibrium and under hydrostatic strain was investigated using projected (PDOS) and overlap population weighted density of states (OPWDOS). It was found that OPWDOS in the valence and conduction band energy regions is of mostly bonding and anti-bonding type, respectively. ZORA results were compared with Augmented

Plane Wave plus Local Orbitals method (APW+lo) and a good agreement between the two sets of calculations was established. Viability and robustness of the ZORA Hamiltonian for the investigation of electronic and structural properties of semiconductors was reaffirmed.

## V. ACKNOWLEDGMENT

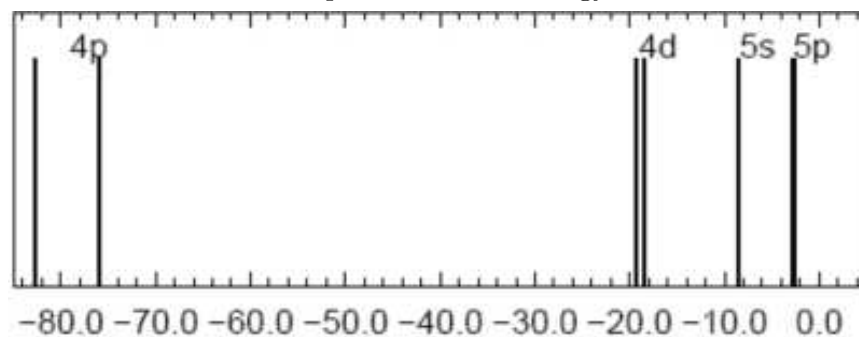
The author acknowledges support by the NRC-NSERC-BDC Nanotechnology project, QuantumWorks, NRC-CNRS CRP and CIFAR. The author thanks Prof. Pawel Hawrylak for stimulating discussions. The author thanks Dr. Maxim Shishkin for reading the manuscript and making useful suggestions.

- 
- [1] L. Jacak, P. Hawrylak, and A. Wojs, *Quantum Dots* (Springer-Verlag, Berlin, 1998).
  - [2] D. Dalacu, M. E. Reimer, S. Frederick, D. Kim, J. Lapointe, P. J. Poole, G. C. Aers, R. L. Williams, W. R. McKinnon, M. Korkusinski, and P. Hawrylak, *Laser and Photonics Reviews* **4**, 283 (2010).
  - [3] A. J. Shields, *Nature Photonics* **1**, 215 (2007).
  - [4] R. M. Stevenson, R. J. Young, P. Atkinson, K. Cooper, D. A. Ritchie, and A. J. Shields, *Nature* **439**, 179 (2006).
  - [5] N. Akopian, N. H. Lindner, E. Poem, Y. Berlatzky, J. Avron, D. Gershoni, B. D. Gerardot, and P. M. Petroff, *Phys. Rev. Lett.* **96**, 130501 (2006).
  - [6] A. Greilich, M. Schwab, T. Berstermann, T. Auer, R. Oulton, D. R. Yakovlev, M. Bayer, V. Stavarache, D. Reuter, and A. Wieck, *Phys. Rev. B* **73**, 045323 (2006).
  - [7] P. Hohenberg and W. Kohn, *Phys. Rev.* **136**, B864 (1964).
  - [8] W. Kohn and L. J. Sham, *Phys. Rev.* **140**, A1133 (1965).
  - [9] U. von Barth and L. Hedin, *J. Phys. C: Solid State Phys.* **5** (1972).
  - [10] A. Mujica, A. Rubio, A. Muñoz, and R. J. Needs, *Rev. Mod. Phys.* **75**, 863 (2003).
  - [11] C. G. Van de Walle, *Phys. Rev. B* **39**, 1871 (1989).
  - [12] S.-H. Wei and A. Zunger, *Appl. Phys. Lett.* **72**, 2011 (1998).
  - [13] S.-H. Wei and A. Zunger, *Phys. Rev. B* **60**, 5404 (1999).
  - [14] Y.-H. Li, X. G. Gong, and S.-H. Wei, *Phys. Rev. B* **73**, 245206 (2006).

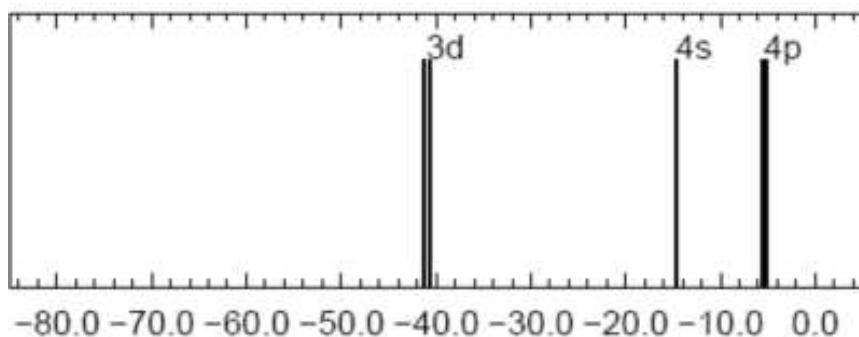
- [15] Y.-H. Li, A. Walsh, S. Chen, W.-J. Yin, J.-H. Yang, J. Li, J. L. F. Da Silva, X. G. Gong, and S.-H. Wei, *Appl. Phys. Lett.* **94**, 212109 (2009).
- [16] E. Sjöstedt, L. Nordström, and D. J. Singh, *Solid State Comm.* **114**, 15 (2000).
- [17] G. K. H. Madsen, P. Blaha, K. Schwarz, E. Sjöstedt, and L. Nordström, *Phys. Rev. B* **64**, 195134 (2001).
- [18] D. Singh, *Plane waves, pseudopotentials and the LAPW method* (Kluwer Academic, 1994).
- [19] K. Schwarz, P. Blaha, and G. K. H. Madsen, *Comp. Phys. Commun.* (2001).
- [20] G. te Velde, *Ph. D. Thesis, Vrije Universiteit, Amsterdam* (1990).
- [21] G. te Velde and E. J. Baerends, *Phys. Rev. B* **44**, 7888 (1991).
- [22] G. te Velde, E. J. Baerends, P. H. T. Philipsen, G. Wiesenekker, J. A. Groeneveld, J. A. Berger, P. L. de Boeij, R. Klooster, F. Kootstra, P. Romaniello, J. G. Snijders, E. S. Kadantsev, and T. Ziegler, *Band 2008.01, SCM: Theoretical Chemistry, Vrije Universiteit, Amsterdam, The Netherlands*.
- [23] E. van Lenthe and J. G. Baerends, E. J. and Snijders, *J. Chem. Phys.* **99**, 4597 (1993).
- [24] E. van Lenthe, E. J. Baerends, and E. J. Snijders, *J. Chem. Phys.* **101**, 9783 (1994).
- [25] E. van Lenthe, J. G. Snijders, and E. J. Baerends, *J. Chem. Phys.* **105**, 6505 (1996).
- [26] E. van Lenthe, R. van Leeuwen, E. J. Baerends, and J. G. Snijders, *Int. J. of Quant. Chem.* **57**, 281 (1996).
- [27] E. van Lenthe, A. E. Ehlers, and E. J. Baerends, *J. Chem. Phys.* **110**, 8943 (1999).
- [28] E. S. Kadantsev and T. Ziegler, *J. Phys. Chem. A* **113**, 1327 (2009).
- [29] P. H. T. Philipsen, E. van Lenthe, and E. J. Baerends, *Phys. Rev. B* **56**, 13556 (1997).
- [30] R. A. Olsen, P. H. T. Philipsen, and E. J. Baerends, *J. of Chem. Phys.* **119**, 4522 (2003).
- [31] P. Romaniello and P. L. de Boeij, *J. Chem. Phys.* **122**, 164303 (2005).
- [32] P. Romaniello and P. de Boeij, *J. Chem. Phys.* **127**, 174111 (2007).
- [33] F. Kootstra, P. L. de Boeij, and J. G. Snijders, *Phys. Rev. B* **62**, 7071 (2000).
- [34] Hoffmann, *Rev. Mod. Phys.* **60**, 602 (1988).
- [35] <http://exciting.sourceforge.net/>; version 0.9.151.
- [36] P. M. Boerrigter, G. te Velde, and E. J. Baerends, *Int. J. Quantum Chem.* **33**, 87 (1988).
- [37] G. Wiesenekker and E. J. Baerends, *J. of Phys.: Condensed Matter* **3**, 6721 (1991).
- [38] G. Wiesenekker, G. te Velde, and E. J. Baerends, *J. of Phys.: Condensed Matter* **21**, 4263 (1988).

- [39] S. H. Vosko, L. Wilk, and M. Nusair, *Can. J. Phys.* **58**, 1200 (1980).
- [40] J. P. Perdew and Y. Wang, *Phys. Rev. B* **45** (1992).
- [41] F. D. Murnaghan, *Am. J. Math.* **49** (1937).
- [42] R. S. Mulliken, *J. Chem. Phys.* **23**, 1833 (1955).
- [43] F. M. Bickelhaupt, N. J. R. van Eikema Hommes, C. Fonseca Guerra, and E. J. Baerends, *Organometallics* **15**, 2923 (1996).
- [44] P. van den Hoek, E. Baerends, and R. van Santen, *J. Phys. Chem.* **93**, 6469 (1989).
- [45] O. Madelung, ed., *Landolt-Börnstein, New Series*, vol. 22a (Springer-Verlag, Berlin, 1987).
- [46] R. J. Nelmes and M. I. McMahon, *Semicond. Semimetals* **54**, 145 (1998).
- [47] M. I. McMahon and R. J. Nelmes, *Phys. Rev. Lett.* **78**, 3697 (1997).
- [48] Y. G. Vohra, S. T. Weir, and A. L. Ruoff, *Phys. Rev. B* **31**, 7344 (1985).
- [49] C. S. Menoni and I. L. Spain, *Phys. Rev. B* **35**, 7520 (1987).
- [50] R. J. Nelmes, M. I. McMahon, N. G. Wright, D. R. Allan, H. Liu, and J. S. Loveday, *J. Phys. Chem. Solids* **56**, 539 (1995).
- [51] N. E. Christensen, *Phys. Rev. B* **33**, 5096 (1986).
- [52] S. B. Zhang and M. L. Cohen, *Phys. Rev. B* **35**, 7604 (1987).
- [53] G. I. Csonka, J. P. Perdew, A. Ruzsinszky, P. H. T. Philipsen, S. Lebègue, J. Paier, O. A. Vydrov, and J. G. Ángyán, *Phys. Rev. B* **79**, 155107 (2009).
- [54] U. von Barth, *Physica Scripta* **T109**, 9 (2004).
- [55] T. Ziegler, J. G. Snijders, and E. J. Baerends, *J. Chem. Phys.* **74**, 1271 (1981).
- [56] F. L. Hirshfeld, *Theor. Chim. Acta* **44**, 129 (1977).
- [57] E. Kadantsev and H. Schmider, *Int. J. Quant. Chem.* **108**, 1 (2008).
- [58] P. Pyykko, *Chem. Rev.* **88**, 563 (1988).

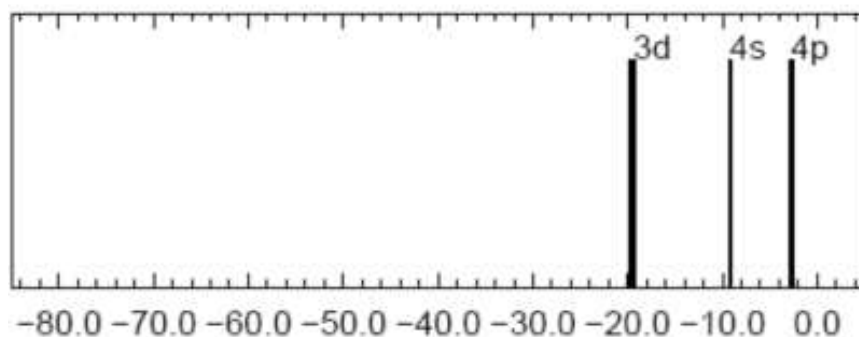
FIG. 1: "Spherical atom" energy levels.



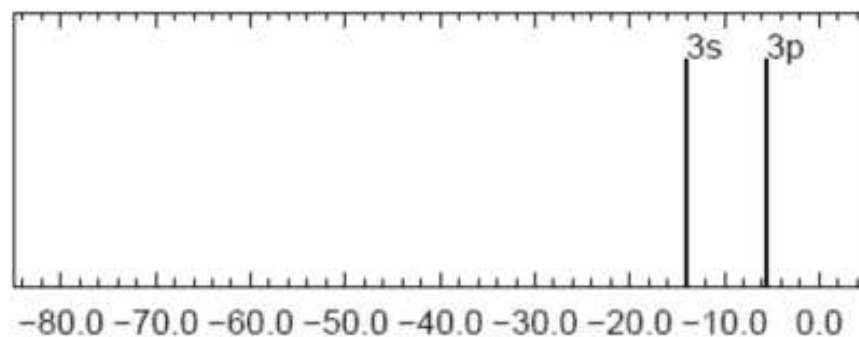
(a) In levels [eV]



(b) As levels [eV]



(c) Ga levels [eV]



(d) P levels [eV]

FIG. 2: LSDA error (%) between KS DFT calculated lattice constant and experimental lattice constants at different “levels of relativity” (FREL - fully relativistic, SREL - scalar relativistic, and NREL - nonrelativistic). LSDA lattice constants (FREL, SREL) underestimate experimental constants. In the case of InAs and InP, the NREL DFT lattice constant is larger than the experimental one which contradicts to the established trend. The experimental lattice constants were determined at the room temperature.

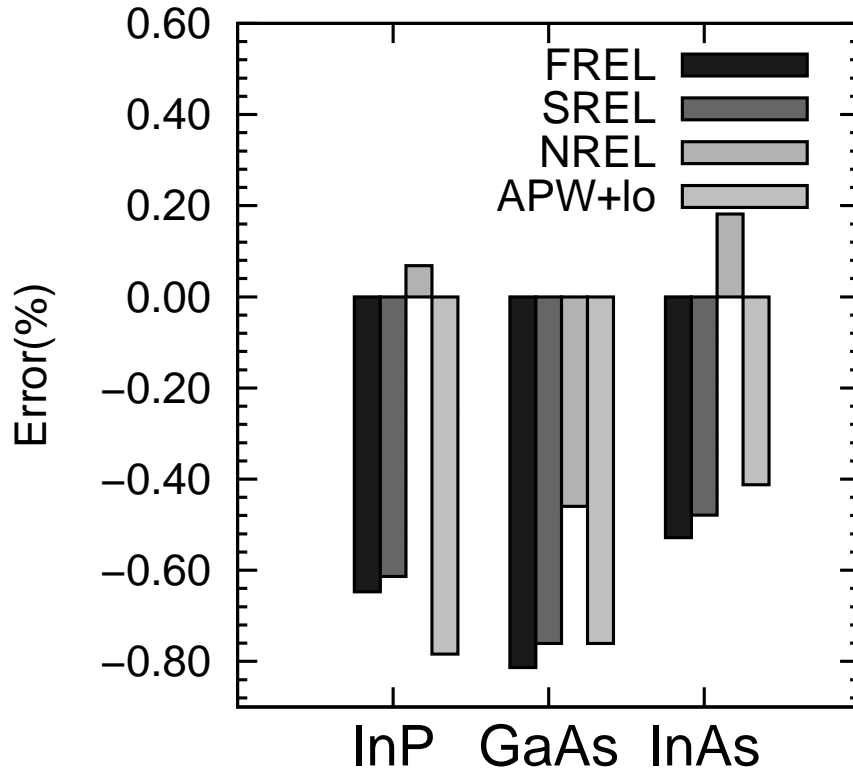


FIG. 3: LSDA bulk modulus calculated at different “levels of relativity” (FREL - fully relativistic, SREL - scalar relativistic, and NREL - nonrelativistic). The LSDA calculations (this work) reproduce the “stiffness” trend  $B_{InAs} < B_{InP} < B_{GaAs}$ .

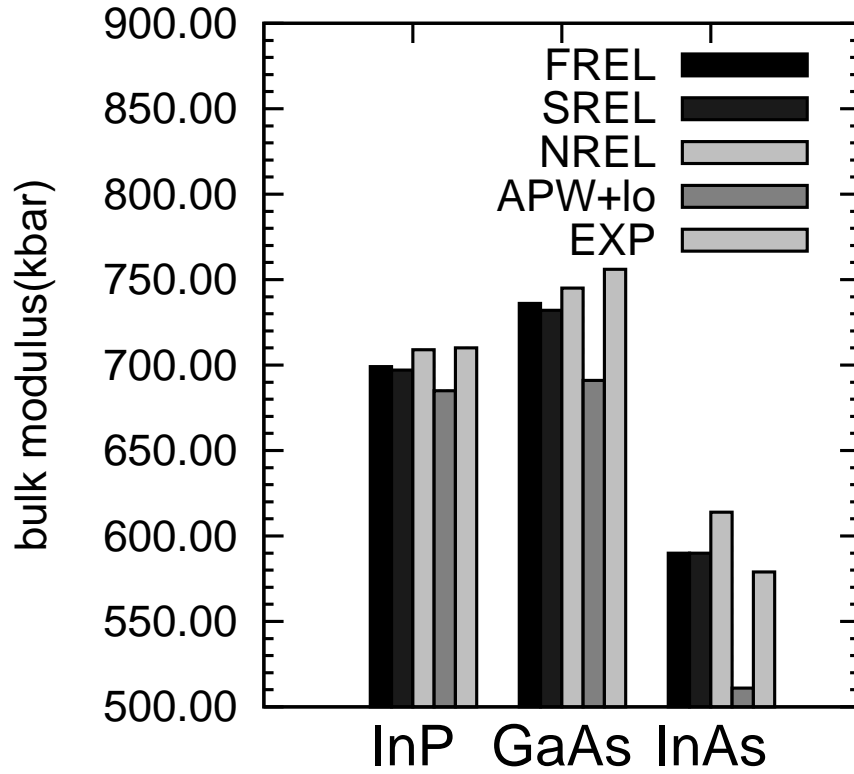


FIG. 4: PDOS in InP. Results of fully relativistic calculations for several lattice constants.

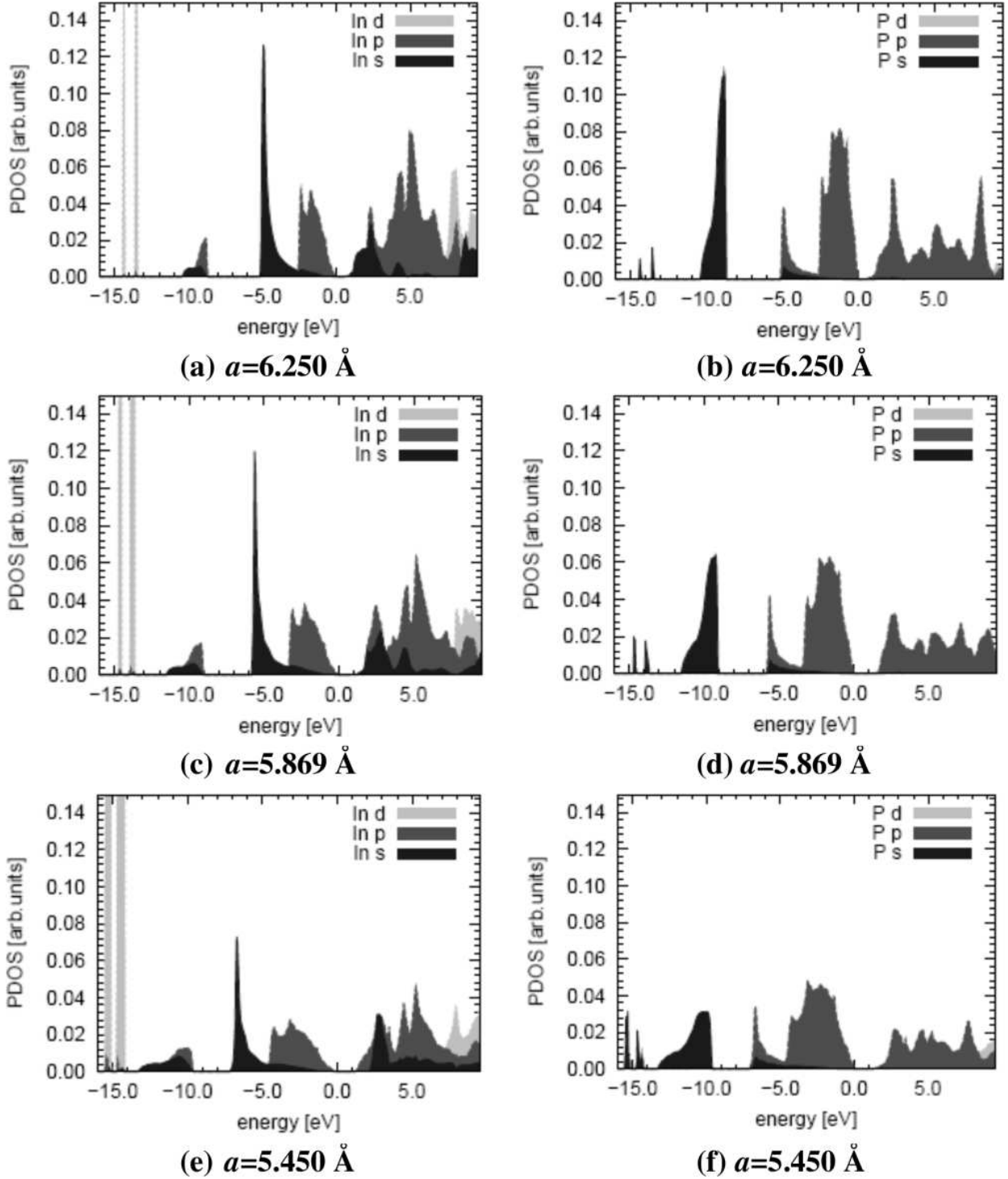


FIG. 5: OPWDOS in InP ( $a = 5.869 \text{ \AA}$ ). Results of scalar relativistic calculations.

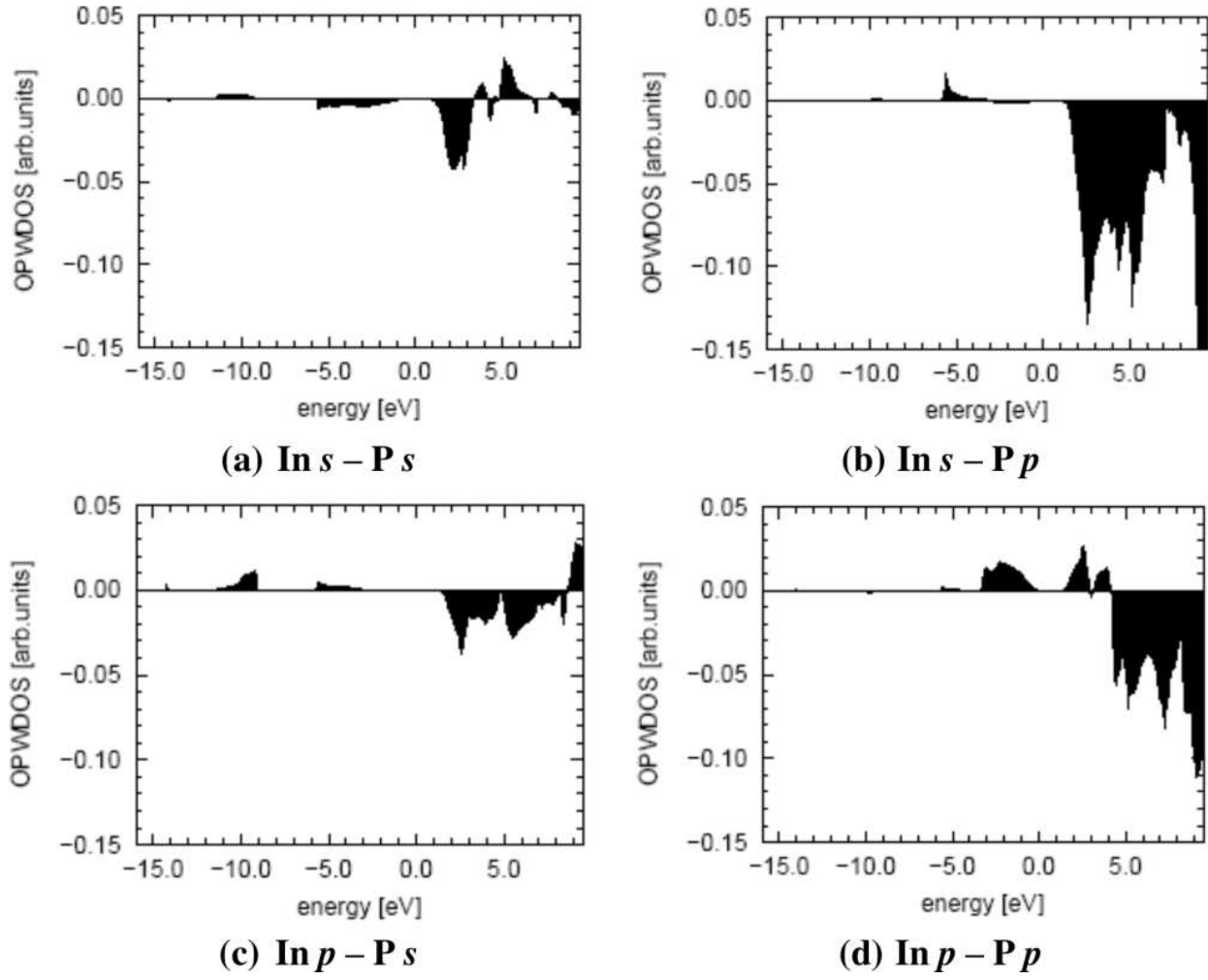


FIG. 6: PDOS in GaAs. Results of fully relativistic calculations for several lattice constants.

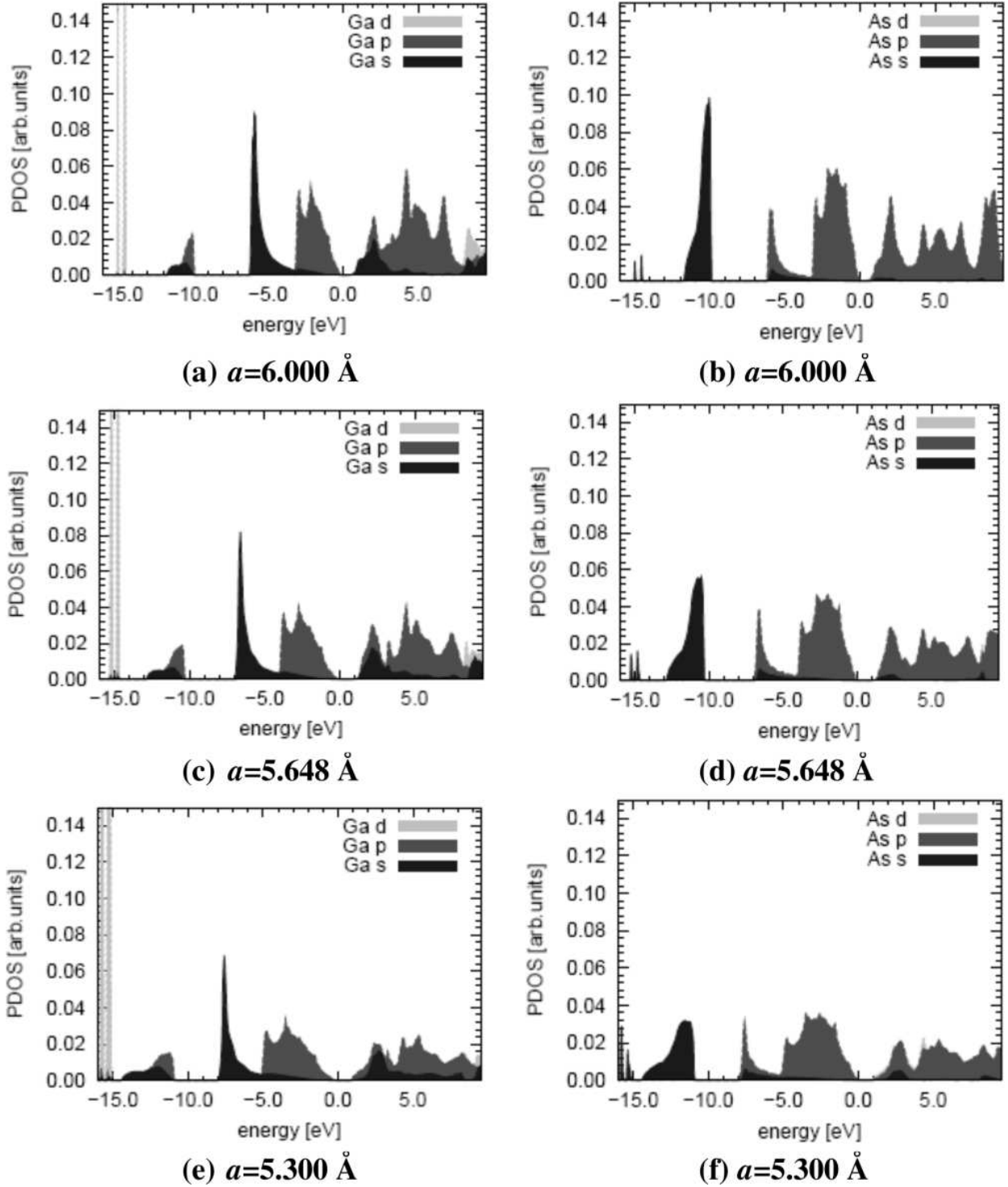


FIG. 7: OPWDOS in GaAs ( $a = 5.648 \text{ \AA}$ ). Results of scalar relativistic calculations.

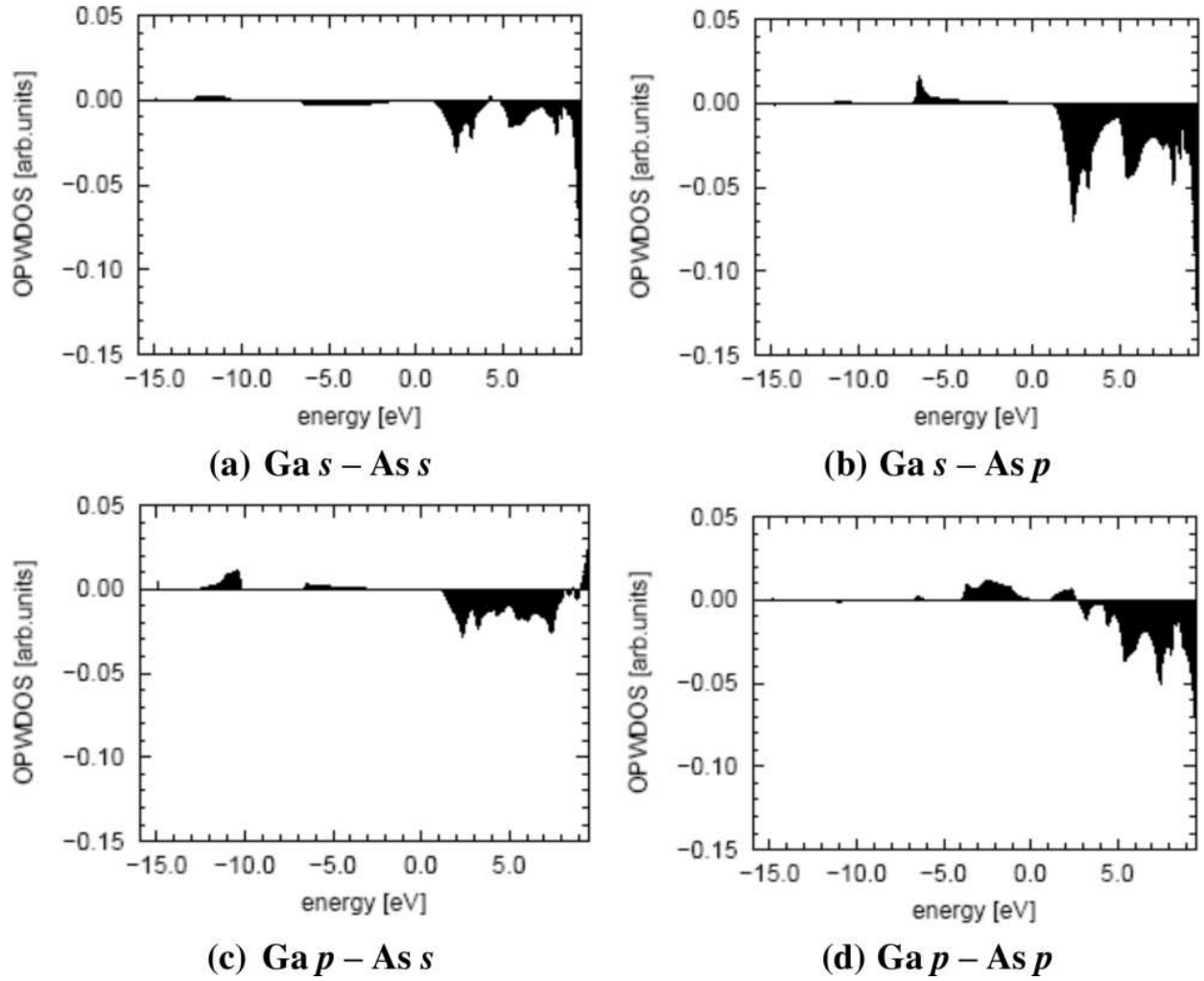


FIG. 8: PDOS in InAs. Results of fully relativistic calculations for several lattice constants.

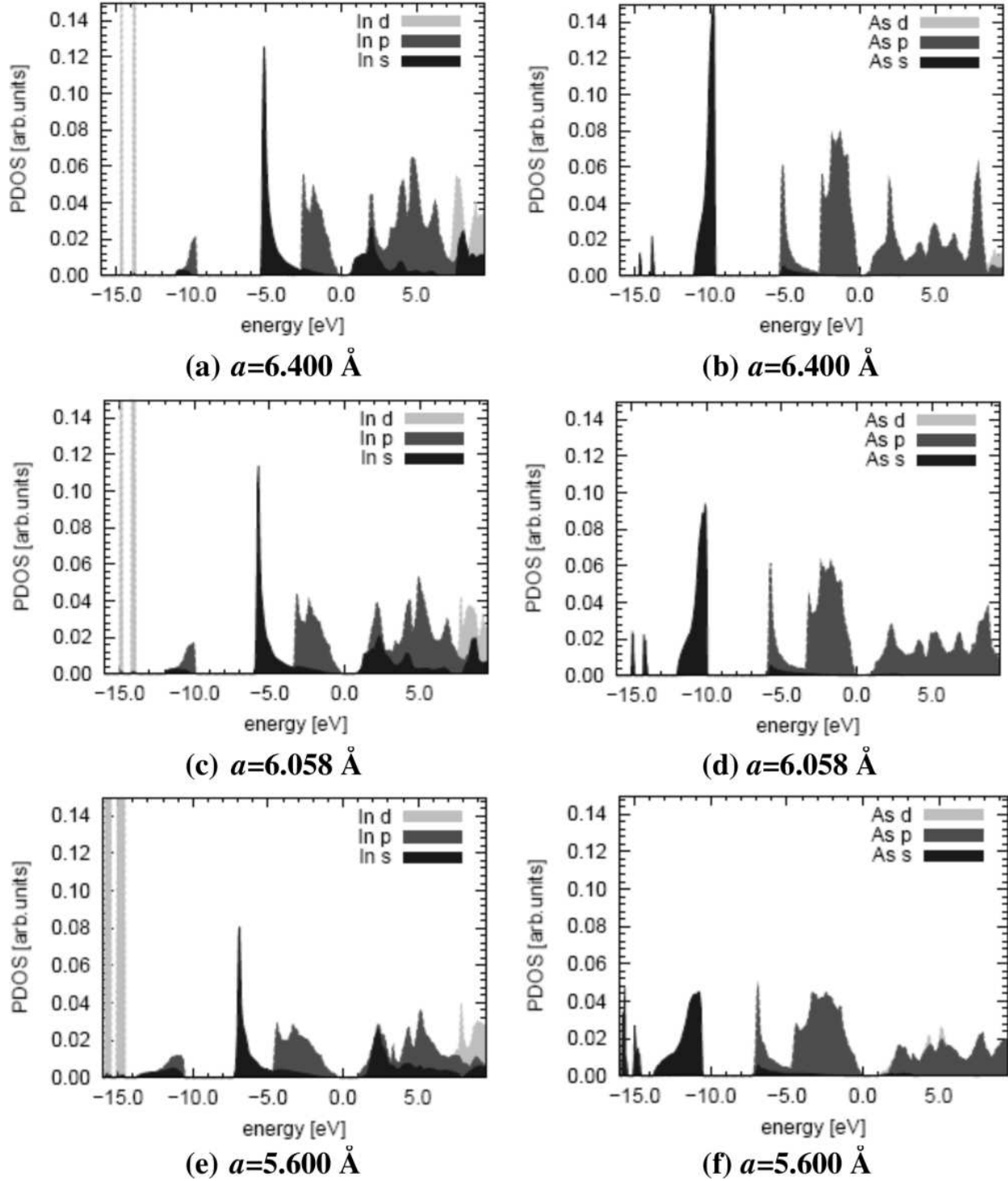


FIG. 9: OPWDOS in InAs ( $a = 6.058 \text{ \AA}$ ). Results of scalar relativistic calculations.

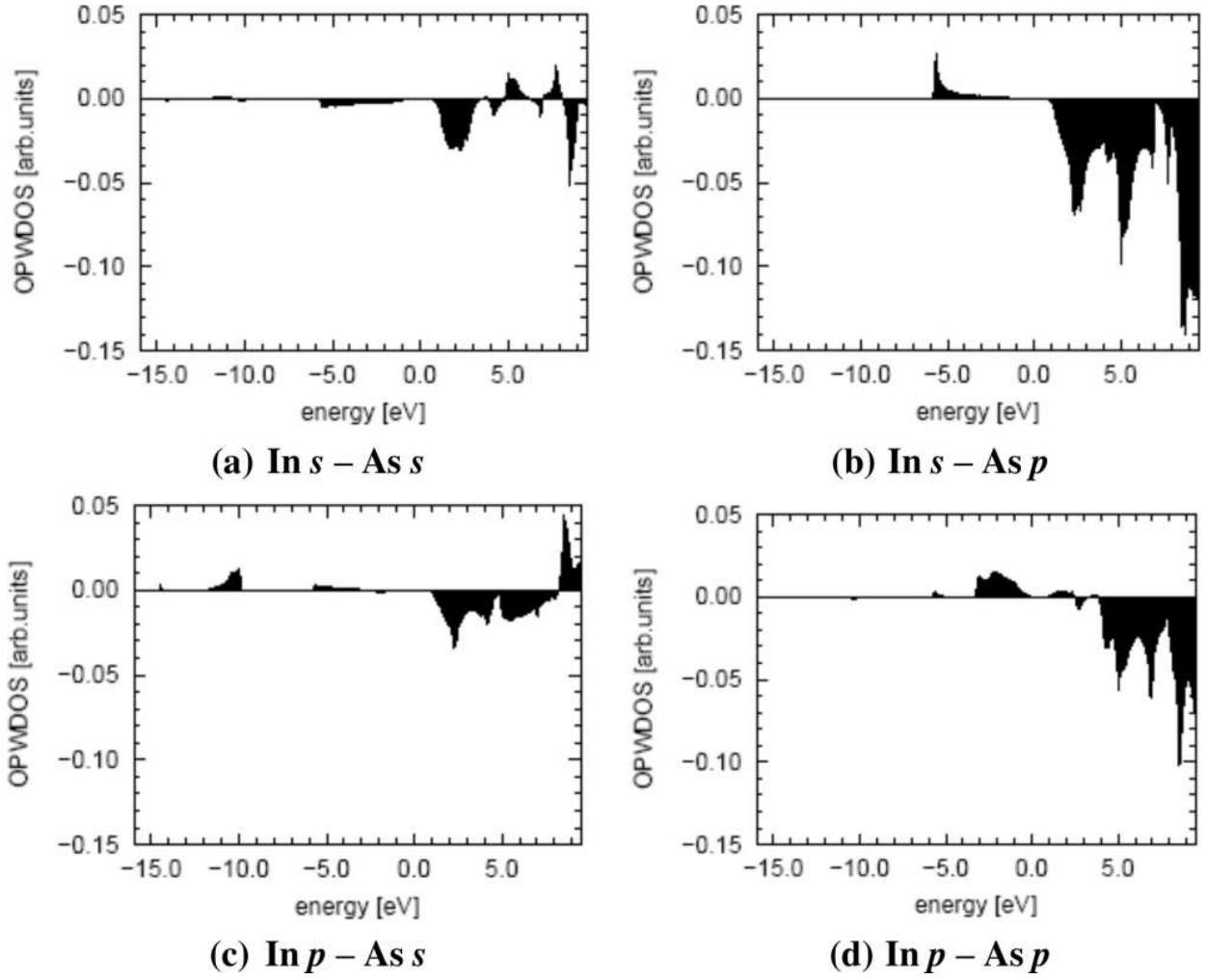


FIG. 10: Band Structure of InP, GaAs, and InAs. Results of scalar relativistic calculations.

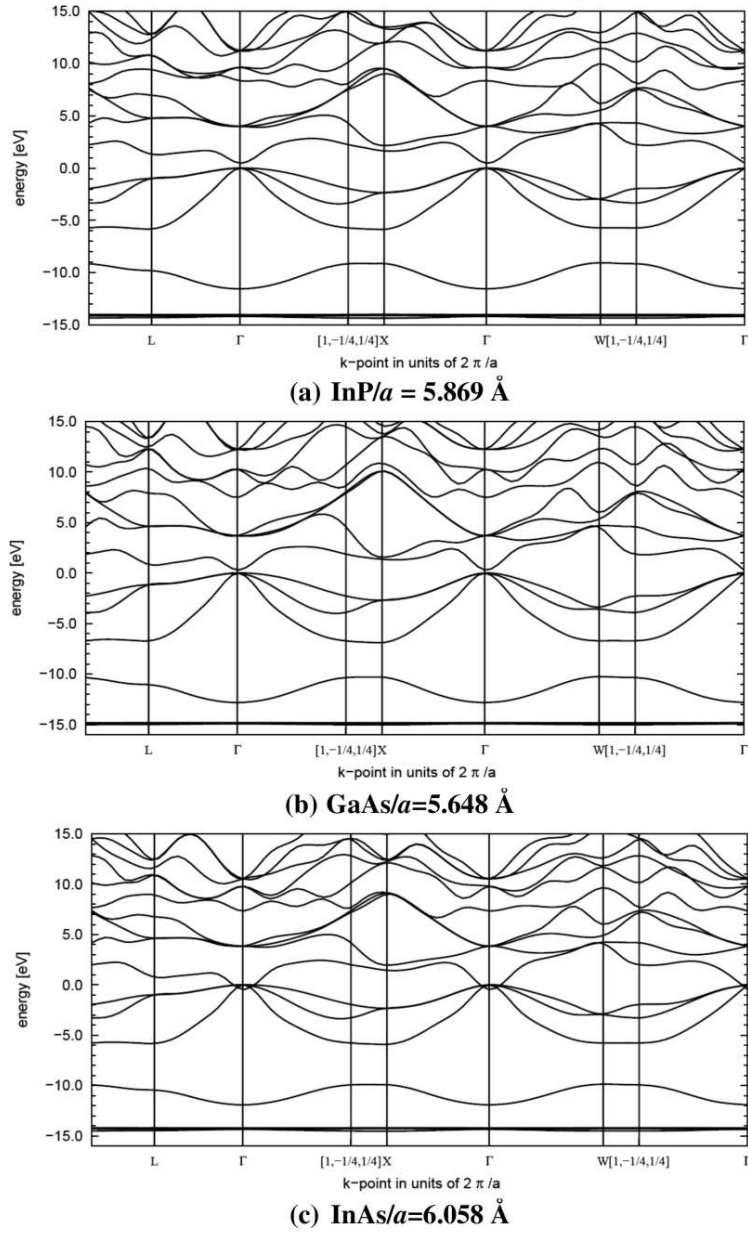
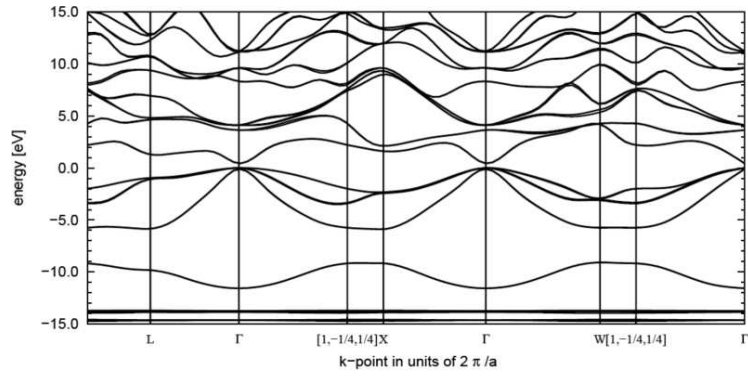
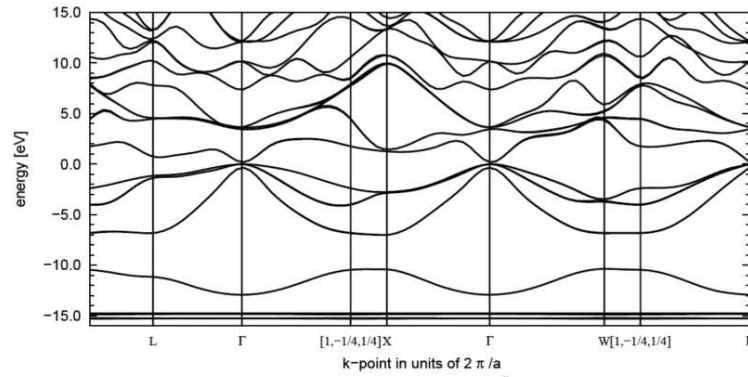


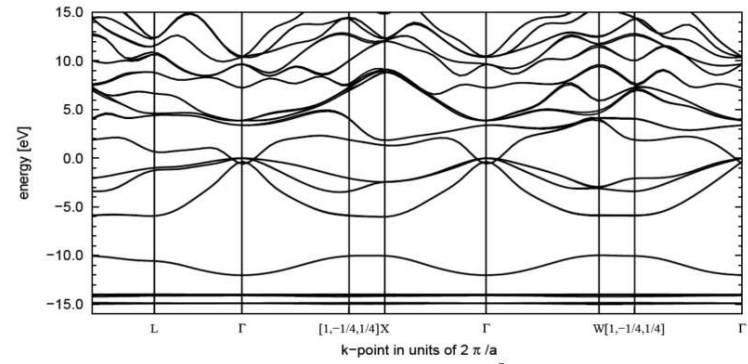
FIG. 11: Band Structure of InP, GaAs, and InAs. Results of fully relativistic calculations.



(a) InP/ $a=5.869 \text{ \AA}$



(b) GaAs/ $a=5.648 \text{ \AA}$



(c) InAs/ $a=6.058 \text{ \AA}$

TABLE I:

Structural parameters of InP, GaAs and InAs IIIA-VA semiconductors (zinc-blende crystal structure). LSDA equilibrium lattice constant  $a_{eq}$  (Å), bulk moduli  $B$  (kbar=0.1GPa) and pressure derivatives  $B'$ . Experimental values are taken from Ref. [45]. The experimental bulk modulus is computed from the elastic constants  $c_{11}$  and  $c_{12}$  as  $B = (c_{11} + 2c_{12})/3$ .

Method	$a_{eq}$ (Å)	$B$ (kbar)	$B'$
InP			
ZORA FREL	5.831	699	4.5
ZORA SREL	5.833	697	4.5
NREL	5.873	709	4.4
APW+lo	5.823	685	4.4
EXP.	5.869 <sup>a</sup>	710 <sup>d</sup>	
GaAs			
ZORA FREL	5.607	736	4.4
ZORA SREL	5.610	732	4.4
NREL	5.627	745	4.5
APW+lo	5.610	691	4.4
EXP.	5.653 <sup>b</sup>	756 <sup>d</sup>	
InAs			
ZORA FREL	6.026	590	4.7
ZORA SREL	6.029	590	4.8
NREL	6.069	614	4.4
APW+lo	6.033	511	4.6
EXP.	6.058 <sup>c</sup>	579 <sup>d</sup>	

Experimental temperature: <sup>a</sup>T=291.15 K, <sup>b</sup>T=298.15 K, <sup>c</sup>T=300 K, <sup>d</sup>room temperature

TABLE II:

Parameters of electronic structure for InP, GaAs, and InAs IIIA-VA semiconductors (zinc-blende crystal structure). All energies are in eV.  $E_{gap}$  – energy gaps for transition between high-symmetry points of the Brillouin zone,  $\Delta_{SO}^{\Gamma}$  and  $\Delta_{SO}^L$  – magnitude of spin-orbital splitting at the top of the valence band at  $\Gamma$  and  $L$  points,  $E_d^{\Gamma}$  –  $d$  band position at the  $\Gamma$  point,  $\delta E_d^{\Gamma}$  –  $d$  band width at the  $\Gamma$  point, and  $UVBW$  - the upper valence band width.

Method	$E_{gap}^{\Gamma_V \rightarrow \Gamma_C}$	$E_{gap}^{\Gamma_V \rightarrow X_C}$	$E_{gap}^{\Gamma_V \rightarrow L_C}$	$\Delta_{SO}^{\Gamma}$	$\Delta_{SO}^L$	$E_d^{\Gamma}$	$\delta E_d^{\Gamma}$	UVBW
InP								
ZORA FREL	0.437	1.606	1.292	0.108	0.120	-14.19	0.89	5.89
ZORA SREL	0.475	1.644	1.330	0.0	0.0	-14.09	0.16	5.85
NREL	1.014	1.590	1.781	0.0	0.0	-15.07	0.14	5.51
APW+lo	0.416	1.575	1.257	0.100	0.112	-14.21	0.89	5.90
EXP.	1.420	2.384	2.014	0.110	0.130			
GaAs								
ZORA FREL	0.196	1.257	0.748	0.349	0.213	-15.01	0.48	7.00
ZORA SREL	0.313	1.372	0.865	0.0	0.0	-14.85	0.08	6.89
NREL	0.965	1.418	1.197	0.0	0.0	-15.38	0.08	6.69
APW+lo	0.173	1.240	0.735	0.341	0.209	-15.02	0.48	6.99
EXP.	1.520	1.979	1.819	0.340	0.220			
InAs								
ZORA FREL	-0.577	1.325	0.661	0.363	0.262	-14.46	0.88	6.02
ZORA SREL	-0.459	1.444	0.784	0.0	0.0	-14.27	0.13	5.90
NREL	0.405	1.453	1.337	0.0	0.0	-15.26	0.11	5.49
APW+lo	-0.594	1.325	0.653	0.351	0.250	-14.48	0.88	6.03
EXP.	0.420	2.24	1.133	0.380	0.267			

TABLE III:

Orbital populations of the band edges in InP, GaAs, and InAs semiconductors (zinc-blende crystal structure) in high-symmetry points of the Brillouin zone at the equilibrium lattice constants. SO – split-off band, LH – light hole band, HH – heavy hole band, and CB – conduction band minimum. ZORA FREL LSDA calculation.

InP												
	$\Gamma$				$X$				$L$			
	<i>In.s</i>	<i>In.p</i>	<i>P.s</i>	<i>P.p</i>	<i>In.s</i>	<i>In.p</i>	<i>P.s</i>	<i>P.p</i>	<i>In.s</i>	<i>In.p</i>	<i>P.s</i>	<i>P.p</i>
SO	0.000	0.112	0.000	0.809	0.619	0.000	0.000	0.327	0.451	0.328	0.042	0.179
LH	0.000	0.072	0.000	0.878	0.000	0.360	0.000	0.630	0.000	0.237	0.000	0.752
HH	0.000	0.072	0.000	0.878	0.000	0.339	0.000	0.645	0.000	0.209	0.000	0.786
CB	0.920	0.000	0.067	0.000	0.000	0.621	0.030	0.000	0.430	0.252	0.014	0.234
GaAs												
	$\Gamma$				$X$				$L$			
	<i>Ga.s</i>	<i>Ga.p</i>	<i>As.s</i>	<i>As.p</i>	<i>Ga.s</i>	<i>Ga.p</i>	<i>As.s</i>	<i>As.p</i>	<i>Ga.s</i>	<i>Ga.p</i>	<i>As.s</i>	<i>As.p</i>
SO	0.000	0.118	0.000	0.755	0.523	0.000	0.000	0.402	0.452	0.352	0.015	0.183
LH	0.000	0.128	0.000	0.738	0.000	0.435	0.000	0.539	0.000	0.294	0.000	0.661
HH	0.000	0.128	0.000	0.738	0.000	0.453	0.000	0.524	0.000	0.279	0.000	0.636
CB	0.728	0.000	0.216	0.000	0.000	0.556	0.040	0.000	0.305	0.298	0.092	0.130
InAs												
	$\Gamma$				$X$				$L$			
	<i>In.s</i>	<i>In.p</i>	<i>As.s</i>	<i>As.p</i>	<i>In.s</i>	<i>In.p</i>	<i>As.s</i>	<i>As.p</i>	<i>In.s</i>	<i>In.p</i>	<i>As.s</i>	<i>As.p</i>
SO	0.000	0.100	0.000	0.829	0.610	0.000	0.000	0.303	0.485	0.279	0.019	0.217
LH	0.000	0.081	0.000	0.843	0.000	0.339	0.000	0.637	0.000	0.242	0.000	0.750
HH	0.000	0.081	0.000	0.843	0.000	0.360	0.000	0.611	0.000	0.210	0.000	0.780
CB	0.897	0.000	0.093	0.000	0.000	0.605	0.039	0.000	0.354	0.347	0.026	0.143

TABLE IV:

Relative volume deformation potentials  $a_V$  (eV) for InP, GaAs, and InAs IIIA-VA semiconductors (zinc-blende crystal structure) for specific transitions. The different signs of the deformation potential is attributed to the “different nature” of the conduction band minimum. Experimental volume deformation potentials are obtained from the direct band gap pressure dependence coefficient and bulk modulus.

Method	$a_V^{\Gamma_V \rightarrow \Gamma_C}$	$a_V^{\Gamma_V \rightarrow X_C}$	$a_V^{\Gamma_V \rightarrow L_C}$
InP			
ZORA FREL	-5.44	1.64	-2.42
ZORA SREL	-5.45	1.64	-2.42
NREL	-5.12	1.60	-2.65
APW+lo	-5.44	1.64	-2.40
EXP.	-5.7		
GaAs			
ZORA FREL	-7.46	1.83	-2.78
ZORA SREL	-7.52	1.79	-2.82
NREL	-7.79	1.81	-3.06
APW+lo	-7.41	1.84	-2.74
EXP.	-8.0,-9.2		
InAs			
ZORA FREL	-5.04	1.59	-2.11
ZORA SREL	-5.09	1.56	-2.15
NREL	-5.11	1.51	-2.58
APW+lo	-5.01	1.59	-2.09
EXP.	-6.6		

TABLE V:

Cartesian coordinates of special  $\mathbf{k}$ -points used to construct the band structure plots (special  $\mathbf{k}$ -points are shown with vertical lines).  $a$  - lattice constant.

Symbol	Coordinates
	$\frac{2\pi}{a} [1, -1/4, 1/4]$
$L$	$\frac{2\pi}{a} [1/2, -1/2, 1/2]$
$\Gamma$	$\frac{2\pi}{a} [0, 0, 0]$
	$\frac{2\pi}{a} [1, -1/4, 1/4]$
$X$	$\frac{2\pi}{a} [1, 0, 0]$
$\Gamma$	$\frac{2\pi}{a} [0, 0, 0]$
$W$	$\frac{2\pi}{a} [1, 0, 1/2]$
	$\frac{2\pi}{a} [1, -1/4, 1/4]$
$\Gamma$	$\frac{2\pi}{a} [0, 0, 0]$